

The ALMA-PILS survey: propyne (CH_3CCH) in IRAS 16293–2422

H. Calcutt¹, E. R. Willis², J. K. Jørgensen³, P. Bjerkeli¹, N. F. W. Ligterink⁴, A. Coutens⁵, H. S. P. Müller⁶, R. T. Garrod², S. F. Wampfler⁴, M. N. Drozdovskaya⁴

¹Department of Space, Earth and Environment, Chalmers University of Technology, 41296, Gothenburg, Sweden, e-mail: hannah.calcutt@chalmers.se

²Departments of Chemistry and Astronomy, University of Virginia, Charlottesville, VA 22904, USA

³Niels Bohr Institute, University of Copenhagen

Øster Voldgade 5–7, DK-1350 Copenhagen K., Denmark

⁴Center for Space and Habitability, University of Bern, Gesellschaftsstrasse 6, CH-3012 Bern, Switzerland

⁵Laboratoire d'Astrophysique de Bordeaux, Univ. Bordeaux, CNRS, B18N, allée Geoffroy Saint-Hilaire, 33615 Pessac, France

⁶I. Physikalisches Institut, Universität zu Köln, Zùlpicher Str. 77, 50937 Köln, Germany

Received

ABSTRACT

Context. Propyne (CH_3CCH), also known as methyl acetylene, has been detected in a variety of environments, from Galactic star-forming regions to extragalactic sources. Such molecules are excellent tracers of the physical conditions in star-forming regions, allowing the temperature and density conditions surrounding a forming star to be determined.

Aims. This study explores the emission of CH_3CCH in the low-mass protostellar binary, IRAS 16293–2422, examining the spatial scales traced by this molecule, as well as its formation and destruction pathways.

Methods. Atacama Large Millimeter/submillimeter Array (ALMA) observations from the Protostellar Interferometric Line Survey (PILS) are used to determine the abundances and excitation temperatures of CH_3CCH towards both protostars. This data allows us to explore spatial scales from 70 to 2400 au. This data is also compared with the three-phase chemical kinetics model MAGICKAL, to explore the chemical reactions of this molecule.

Results. CH_3CCH is detected towards both IRAS 16293A and IRAS 16293B, and is found to trace the hot corino component around each source in the PILS dataset. Eighteen transitions above 3σ are detected, enabling robust excitation temperatures and column densities to be determined in each source. In IRAS 16293A, an excitation temperature of 90 K and a column density of $7.8 \times 10^{15} \text{ cm}^{-2}$ best fits the spectra. In IRAS 16293B, an excitation temperature of 100 K and $6.8 \times 10^{15} \text{ cm}^{-2}$ best fits the spectra. The chemical modelling finds that in order to reproduce the observed abundances, both gas-phase and grain-surface reactions are needed. The gas-phase reactions are particularly sensitive to the temperature at which CH_4 desorbs from the grains.

Conclusions. CH_3CCH is a molecule whose brightness and abundance in many different regions can be utilised to provide a benchmark of molecular variation with the physical properties of star-forming regions. It is essential when making such comparisons, that the abundances are determined with a good understanding of the spatial scale of the emitting region, to ensure that accurate abundances are derived.

Key words. astrochemistry — stars: formation — stars: protostars — ISM: molecules — ISM: individual objects: IRAS 16293–2422

1. Introduction

Complex organic molecules (COMs) are excellent tracers of the physical conditions in star-forming regions owing to the large number of transitions that span a range of upper energy levels. When they are found in dense environments, they are easily thermalised and can be an excellent probe of the specific temperature conditions surrounding a forming star. One such molecule, propyne (CH_3CCH or $\text{CH}_3\text{C}_2\text{H}$), also known as methyl acetylene, is well-suited for such studies. It is a prolate symmetric top molecule which means that for a given J quantum number, there is a K-ladder which has a large range of energy levels, emitting over a narrow frequency range. It is also relatively abundant in many star-forming regions, and has therefore been detected in a variety of environments from Galactic star-forming regions (e.g. Snyder & Buhl 1973; Bøgelund et al. 2019), to extragalactic sources (Martín et al. 2006; Harada et al. 2018). It is increasingly becoming an important molecule for large comparison studies of chemical diversity among star-forming regions (e.g. Taniguchi

et al. 2018), especially with its ability to link the chemistry of extragalactic sources to local environments, and even planetary atmospheres (e.g. Titan; Cordiner et al. 2015).

Crucially, for CH_3CCH to function as a good reference species in a variety of sources, its column densities and excitation temperatures must be determined robustly. This can pose a significant problem for some sources, which have a very complex physical structure. Observations must be of sufficient angular resolution to ensure that the scales over which CH_3CCH is found are determined. Too high a resolution risks at least some of the emission being filtered out, whereas too low a resolution means beam dilution effects becoming a significant issue when determining column densities and excitation temperatures.

One such observationally complex source is IRAS 16293–2422 (hereafter IRAS 16293). IRAS 16293 is a low-mass protostellar binary, located at a distance of 141 pc (Dzib et al. 2018). A recent survey of IRAS 16293, the Protostellar Interferometric Survey (PILS; Jørgensen et al. 2016), has detected more than 100 molecules from $\sim 10,000$ lines, highlighting the rich molecu-

lar chemistry that can occur in hot corino sources. Its two Class 0 protostars, A and B, are separated by a distance of $5''$ (~ 700 au) and exhibit a rich chemistry in each of their respective hot corinos. IRAS 16293A has a large velocity gradient across a disk-like structure with a near to edge-on morphology, whereas IRAS 16293B has a face-on morphology showing little velocity gradient across the source (Pineda et al. 2012; Jacobsen et al. 2018). IRAS 16293A has even been suggested to be a proto-binary system, with multi epoch continuum observations showing that it contains two continuum peaks (Chandler et al. 2005; Pech et al. 2010; Hernández-Gómez et al. 2019). An overview of the literature on this source can be found in Jørgensen et al. (2016).

Propyne has been detected in IRAS 16293 previously by Cazaux et al. (2003) with the IRAM 30 m telescope, and was attributed to the cold gas component, with an excitation temperature of 25 K. Recent work by Andron et al. (2018), with further IRAM 30 m observations, constrained the emission of propyne to the outer part of envelope, at around 2000 au and an excitation temperature of 25 K, based on radiative transfer modelling of their observations.

In this paper, the emission of propyne in both IRAS 16293A and IRAS 16293B is investigated, using higher angular resolution data than has previously been used. The results from this observational analysis are then compared to the results of chemical modelling of the IRAS 16293 system. The observations are presented in Section 2, and details of the results and analysis are presented in Section 3. In Section 4, details of the chemical modelling are given and in Section 5 the wider impact of the results from this study are discussed. Finally, the conclusions are presented in Section 6.

2. Observations

The observations used in this study are part of the Protostellar Interferometric Line Survey (PILS), an ALMA spectral line survey of IRAS 16293 (Jørgensen et al. 2016). The survey covers Band 7 between 329.147 and 362.896 GHz, and selected frequency windows in Bands 3 and 6. For the purposes of this study the Band 7 and Band 3 data are used. The Band 7 data are a combination of 12 m array and Atacama Compact Array (ACA) observations, which have been combined to have a restoring beam of $0''.5$ at a spectral resolution of 0.2 km s^{-1} . These data probe scales from 70 au ($0''.5$) to 1820 au ($13''$). The phase centre of the observations is located between the two components of the binary system at $\alpha_{J2000} = 16^{\text{h}}32^{\text{m}}22^{\text{s}}.72$, $\delta_{J2000} = -24^{\circ}28'34''.3$. They reach a sensitivity of about $7 - 10 \text{ mJy beam}^{-1} \text{ channel}^{-1}$, i.e. approximately $\sim 5 \text{ mJy beam}^{-1} \text{ km s}^{-1}$ across the entire frequency range. The Band 3 data cover four basebands, spanning the frequency ranges 89.5–89.7 GHz, 92.8–92.9 GHz, 102.5–102.7 GHz, and 103.2–103.4 GHz. They probe spatial scales of $1.4''$ (196 au) to $17''$ (2380 au) and reach a sensitivity of $\sim 5 \text{ mJy beam}^{-1} \text{ km s}^{-1}$. The spectral resolution of the data is 0.4 km s^{-1} . Further details of the PILS datasets and the reduction and the continuum subtraction procedure can be found in Jørgensen et al. (2016).

3. Observational results and analysis

The PILS data has been used to search for CH_3CCH and its isotopologues towards both IRAS 16293A and IRAS 16293B. Spectra were extracted from two positions, where line emission is bright, does not have strong absorption features and does not

suffer from high continuum optical depth (Coutens et al. 2016, Lykke et al. 2017). The first position is at $\alpha_{J2000} = 16^{\text{h}}32^{\text{m}}22^{\text{s}}.58$, $\delta_{J2000} = -24^{\circ}28'32''.8$. This is offset from the continuum peak position of IRAS 16293B in the south west direction by one beam ($0''.5$, 70 au). The second position is at $\alpha_{J2000} = 16^{\text{h}}32^{\text{m}}22^{\text{s}}.90$, $\delta_{J2000} = -24^{\circ}28'36''.2$. This is offset from the peak continuum position of IRAS 16293A by $0''.6$ (85 au), in the north east direction. Both these positions have been used previously to study the chemistry in both hot corinos (e.g. Ligterink et al. 2017, Calcutt et al. 2018, Manigand et al. 2019) to overcome issues of line blending and absorption contamination which affect the peak continuum position.

Rest frequencies and related information on CH_3CCH , CH_2DCCH and CH_3CCD were taken from the CDMS catalogue (Endres et al. 2016). The CH_3CCH data are based on Cazoli & Puzzarini (2008), Müller et al. (2000) and Müller et al. (2002). The CH_2DCCH and CH_3CCD data are largely based on Le Guennec et al. (1993), with most of the data coming from that source.

A total of 18 lines of CH_3CCH are detected above 3σ towards both IRAS 16293A and IRAS 16293B. There are 5 lines that are not severely blended towards IRAS 16293A and 14 lines that are not severely blended towards IRAS 16293B. There are more blended lines in IRAS 16293A because the lines are wider in this source. ^{13}C and deuterated isotopologues of CH_3CCH were searched for but were not detected in the data. Upper limit column densities for these isotopologues are given in Table 3. The upper limits are determined from $1.05 \times 3 \times \text{RMS} \times \sqrt{\Delta V \times \text{FWHM}}$ to compute the 3σ limit, where 1.05 is a factor to account for a 5% flux calibration uncertainty. Line parameters are used for the brightest lines of each isotopologue that fall in the range of the observations. Line widths of 2 km s^{-1} and 1 km s^{-1} are used for IRAS 16293A and IRAS 16293B, respectively. The CH_3CCH excitation temperature determined in this work is used for the upper limit calculations. The upper limit column densities values are found to be consistent with the isotopic ratios that have been determined in both sources by previous works (e.g. Calcutt et al. 2018; Jørgensen et al. 2018). The spectroscopic information for the CH_3CCH lines that are detected is given in Table 1.

3.1. Column densities and excitation temperatures

In order to determine the best fit column densities and excitation temperatures for CH_3CCH towards both sources, a local thermodynamic equilibrium (LTE) model was fitted to the data. For the large densities seen in the environments close to the two protostars, LTE is a good approximation. The spectral modelling software CASSIS¹ was used to calculate synthetic spectra and determine best fit spectral models, by running a grid of models covering a range of column densities, excitation temperatures, full width at half maximums (FWHM), and V_{peak} values. Column densities were varied between $5 \times 10^{13} - 5 \times 10^{18} \text{ cm}^{-2}$, and excitation temperatures between 80–300 K. FWHM values were varied between $2.0 - 2.6 \text{ km s}^{-1}$ for IRAS 16293A and $0.8 - 1.2 \text{ km s}^{-1}$ for IRAS 16293B. V_{peak} values were varied between $0.8 - 1.2 \text{ km s}^{-1}$ for IRAS 16293A and $2.5 - 2.7 \text{ km s}^{-1}$ for IRAS 16293B. The range in FWHMs and peak velocities modelled was based on previous analysis towards each of the offset

¹ CASSIS has been developed by IRAP-UPS/CNRS: <http://cassis.irap.omp.eu/>.

Table 1. Spectroscopic information for the lines of CH₃CCH detected in IRAS 16293.

Transition	Frequency (GHz)	E_u (K)	A_{ij} (s ⁻¹)	T_{peak} IRAS 16293A K	T_{peak} IRAS 16293B K
6 3 – 5 3	102.53035	82	2.67×10^{-6}	5.54	10.10
6 2 – 5 2	102.54015	46	3.16×10^{-6}	4.93	8.66
6 1 – 5 1	102.54602	24	3.46×10^{-6}	6.76	11.50
6 0 – 5 0	102.54798	17	3.56×10^{-6}	7.49	12.60
20 6 – 19 6	341.50702	432	1.26×10^{-4}	1.66	4.48
20 5 – 19 5	341.57846	353	1.30×10^{-4}	2.06	5.09
20 4 – 19 4	341.63695	288	1.34×10^{-4}	4.28	9.66
20 3 – 19 3	341.68247	237	1.36×10^{-4}	14.10	28.10
20 2 – 19 2	341.71499	201	1.38×10^{-4}	10.90	21.60
20 1 – 19 1	341.73451	179	1.39×10^{-4}	13.70	26.00
20 0 – 19 0	341.74102	172	1.39×10^{-4}	14.70	27.60
21 6 – 20 6	358.57236	449	1.48×10^{-4}	1.54	4.22
21 5 – 20 5	358.64734	370	1.52×10^{-4}	1.90	4.77
21 4 – 20 4	358.70873	305	1.55×10^{-4}	3.93	9.07
21 3 – 20 3	358.75650	254	1.58×10^{-4}	13.00	26.60
21 2 – 20 2	358.79063	218	1.60×10^{-4}	10.10	20.30
21 1 – 20 1	358.81112	197	1.61×10^{-4}	12.60	24.50
21 0 – 20 0	358.81795	189	1.61×10^{-4}	13.60	26.10

positions used in this work (e.g. Calcutt et al. 2018; Manigand et al. 2019). This range covers several velocity channels either side of the previous best fit values to account for lines that might be broader or narrower than previously studied molecules, and molecules which may have a different peak velocity. The reduced χ^2 minimum was then computed to determine the best fit model, assuming a source size of 1''4 and 1''1 for A and B respectively, for the higher upper energy lines in Band 7, and a source size of 1''6 and 1''7 for A and B respectively, for the lower upper energy lines in Band 3. These source sizes are based on fitting a 2D Gaussian to the emission, which is discussed in Section 3.2. The significant spectral density seen in IRAS 16293 means that line blending is an issue within the spectra for both sources A and B. Lines are considered to be severely blended, if the maximum intensity of a line overlaps with the first minimum (i.e. where the intensity of the line falls to zero) of a nearby line (Snyder et al. 2005). Such lines are excluded from the best fit model calculations. Lines of CH₃CCH fall within the range of both the Band 3 and Band 7 datasets. Initially, a fit was performed to each dataset independently, and then a combined dataset was modelled. All of the best fit parameters were similar for each source independent of which dataset was modelled.

The flux calibration errors on the Band 7 dataset were estimated to be better than 5% by Jørgensen et al. (2016). Both the flux calibration error and the root mean square (RMS) are used by CASSIS when determining the best fit model. A larger source of error, however, comes from the quality of the fit of the spectral model to the observational data. Line blending and optically thick lines can significantly impact the quality of the fit. To mitigate this, first an initial grid of models was run on all of the emission lines, and then a second grid of models was performed, where only the optically thin lines ($\tau < 0.2$) were used to determine the best fit model. The errors on the fit parameters were then estimated by varying the N_{tot} and T_{ex} to determine the impact this had on the fit of the observations.

The results from this LTE modelling are given in Table 2 and the spectra and best fit model of the brightest lines in IRAS 16293A and IRAS 16293B are shown in Figure 1. Similar excitation temperatures and abundances are found between both

sources. Towards IRAS 16293A the best fit FWHM and peak velocity is 2.0 km s⁻¹ and 1.0 km s⁻¹ respectively. These values are consistent with previous studies performed at the offset position in IRAS 16293A used in this work (e.g. Calcutt et al. 2018). Towards IRAS 16293B the fitted FWHM of 1.0 km s⁻¹ is the same as has been determined for other molecules analysed as part of the PILS survey (e.g. Lykke et al. 2017). The peak velocity is 2.5 km s⁻¹, which is only 1 channel width (0.2 km s⁻¹) different from the source velocity. Such a small shift in peak velocity was also seen in some oxygen-bearing species in Jørgensen et al. (2018). They also found that molecules detected towards IRAS 16293B fell into two categories depending on the excitation temperature, ‘hot’ (~300 K) and ‘cold’ (~125 K), which correlate with the binding energy of the molecules to the grain-surface, i.e. ‘cold’ molecules sublimate before ‘hot’ molecules. CH₃CCH falls in the category of a ‘cold’ molecule, which is consistent with its binding energy of 4287 K. This value is based on the binding energy of acetylene (C₂H₂), measured by Collings et al. (2004), combined with the binding energy of 2 H atoms. Other estimates of the CH₃CCH binding energy by Behmard et al. (2019) find it to have a value between 4400–4700K.

3.2. Spatial extent

Figure 2 shows the spatial extent for four lines of CH₃CCH towards both sources. The top panels show the spectra of the lines and LTE best fit model towards IRAS 16293B and the bottom panel shows the same towards IRAS 16293A. Each line was chosen because it is a bright, unblended line. The middle panel is a velocity-corrected integrated emission (VINE) map of the line emission. A VINE map is a type of integrated emission map developed to determine the emission from molecules in regions where there are large velocity gradients and a large spectral line density. In such sources, it is difficult to determine a velocity interval to integrate over which does not include emission from other lines. VINE maps use a shifting velocity range to isolate the emission from only the line of interest over every pixel in the map. The shifting velocity range is determined using a velocity map of the source and the line width of the line.

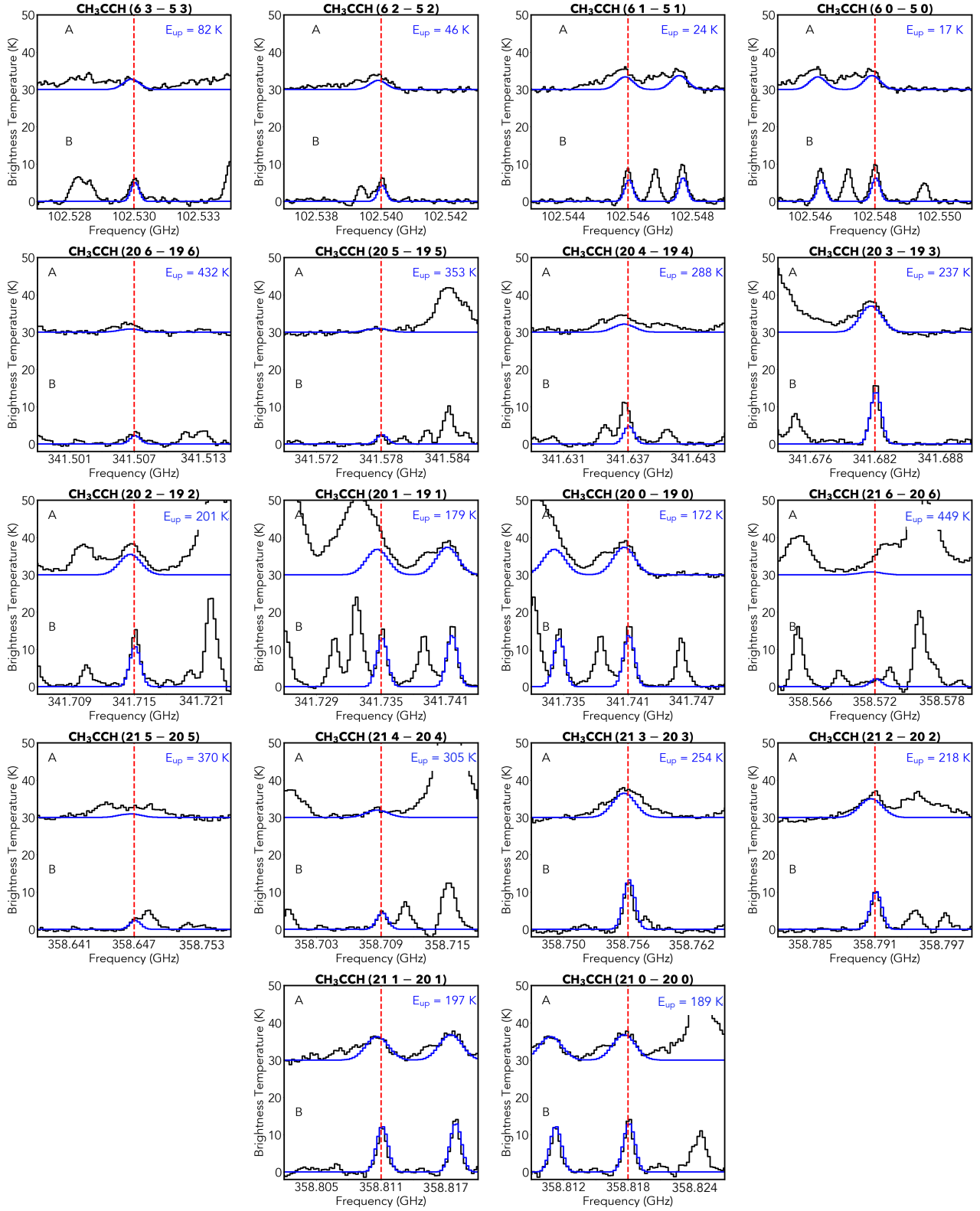


Fig. 1. The lines of CH₃CCH detected in IRAS 16293A and IRAS 16293B (black) overlaid with an LTE spectral model (blue). The upper energy level of each line is given in the top right corner of each plot in K. IRAS 16293A spectra are plotted with an offset of 30 K on the same axis as IRAS 16293B spectra. The red dashed line indicates the systemic velocity for each source.

The velocity interval used is 3.2 km s^{-1} and 1.2 km s^{-1} for IRAS 16293 A and IRAS 16293B, respectively. Further details of how these maps are produced and a comparison between a VINE map and a standard integrated emission map for IRAS 16293

can be found in Calcutt et al. (2018).

CH₃CCH traces the hot corino in both sources in the Band 3 and Band 7 datasets. Table 4 shows the spatial extent of CH₃CCH emission for each transition shown in Figure 2.

Table 2. Excitation temperature (T_{ex}), column density (N_{tot}), the abundance ratio, $N(\text{CH}_3\text{CCH})/N(\text{H}_2)$, $FWHM$, and peak velocity (V_{peak}) in IRAS 16293B and IRAS 16293A.

Source	T_{ex} (K)	N_{tot} (cm^{-2})	$\frac{N(\text{CH}_3\text{CCH})^\dagger}{N(\text{H}_2)}$	$FWHM$ km s^{-1}	V_{peak} km s^{-1}
IRAS 16293A	90 ± 30	$7.8 \pm 1.0 \times 10^{15}$	1.2×10^{-9}	2.0 ± 0.2	1.0 ± 0.2
IRAS 16293B	100 ± 20	$6.8 \pm 0.2 \times 10^{15}$	$< 5.7 \times 10^{-10}$	1.0 ± 0.2	2.5 ± 0.2

Notes. $^\dagger\text{H}_2$ column densities are based on the values determined in Jørgensen et al. (2016) towards IRAS 16293B ($> 1.2 \times 10^{25} \text{ cm}^{-2}$) and values determined in Calcutt et al. (2018) towards IRAS 16293A ($6.3 \times 10^{24} \text{ cm}^{-2}$).

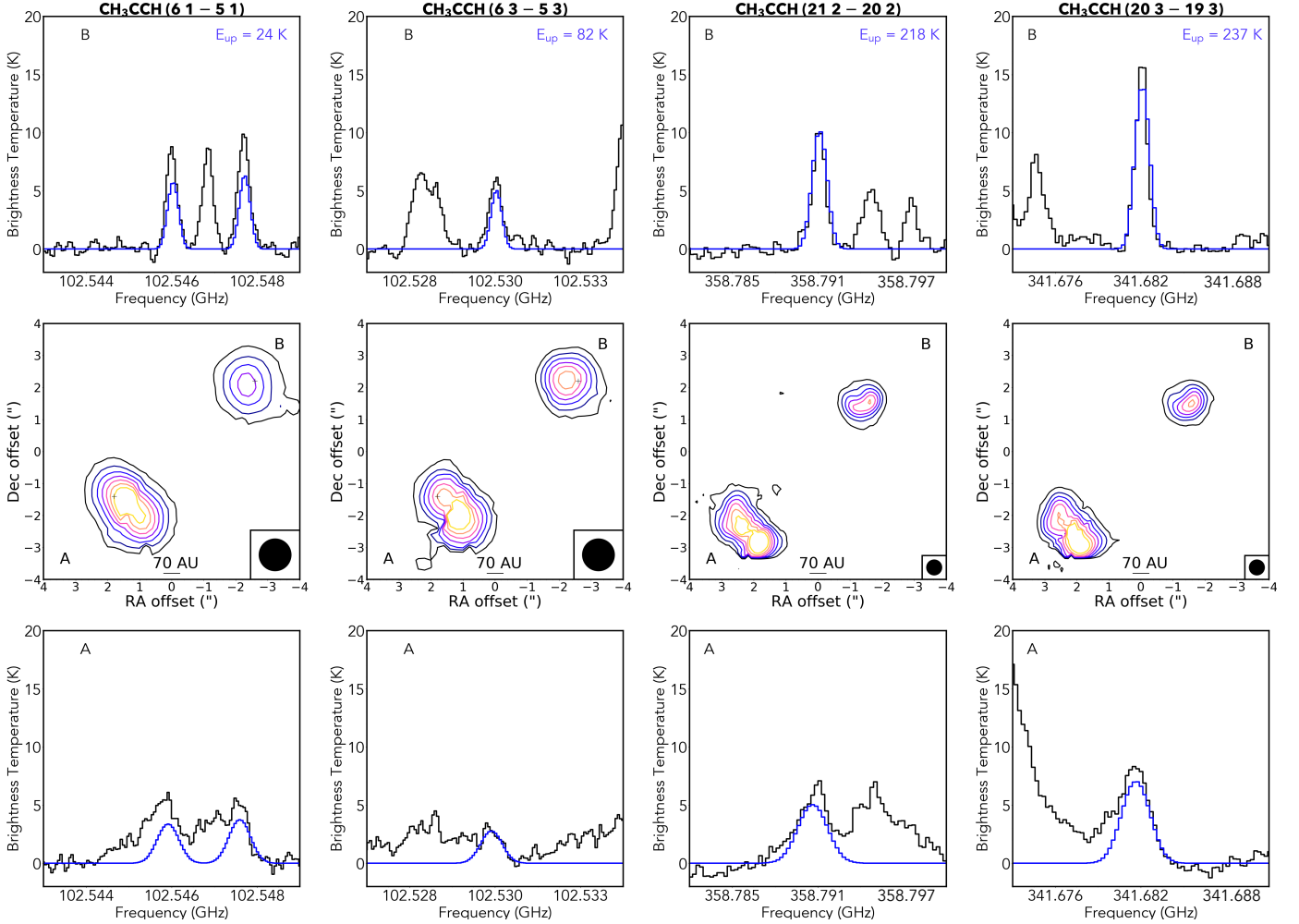


Fig. 2. Emission maps and spectra of the four brightest CH_3CCH lines detected in both the Band 3 and Band 7 datasets. The panels are arranged in order of increasing upper energy level. The top panels show the spectra of the lines (black line) and LTE best fit model (blue line) towards IRAS 16293B and the bottom panel shows the same towards IRAS 16293A. The middle panel shows a velocity-integrated emission map (VINE) map of the emission towards each source. The velocity interval used is 3.2 km s^{-1} and 1.2 km s^{-1} for IRAS 16293 A and IRAS 16293B, respectively. The contours range from 10%–90% of the max flux in each plot in steps of 10%. This corresponds to 8σ – 63σ , 5σ – 40σ , 18σ – 144σ , and 20σ – 167σ for each of the middle panels. The RA and Dec coordinates are given relative to the phase centre of the observations which is the same in both the Band 3 and Band 7 datasets. The shift in position of both sources between the two datasets is to be expected due to the difference in time between the observations, and has been discussed previously (e.g. Peche et al. 2010). The upper energy level of each transition is given in the top right corner of the top panels. The beam size of the observations is given in the bottom right corner of the middle panels.

The values were calculated by determining the FWHM of a 2D-Gaussian fitted to the emission of each source. The emission that is observed is tracing scales smaller than the largest angular scale covered by the data. Lower upper energy level lines are tracing a slightly more extended scale than the higher upper energy level lines. The scale that this emission is tracing is comparable to the scale traced by other complex organic molecules in both A and B, including methyl cyanide (CH_3CN)

and its isotopologues discussed in Calcutt et al. (2018), and methyl formate (CH_3OCHO , Manigand et al. 2019).

Recent analysis by Andron et al. (2018), of CH_3CCH towards this source using IRAM 30m observations, claims CH_3CCH emission on scales of 1700 au. The Band 3 PILS dataset contains six of the same transitions as the IRAM data. The Common Astronomy Software Applications package

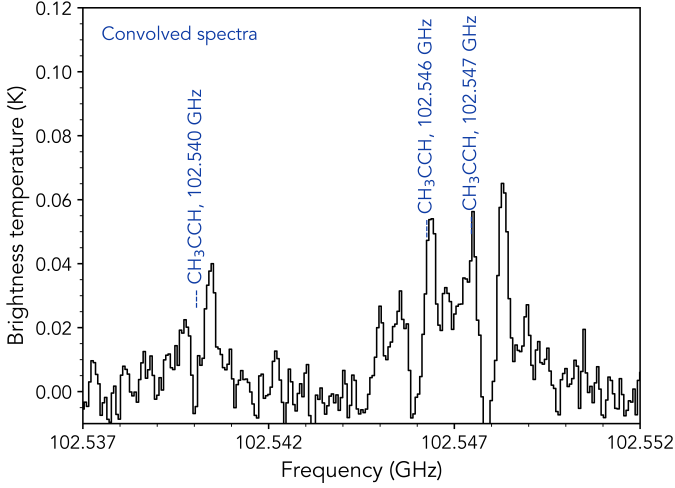


Fig. 3. Spectra of three lines of CH_3CCH extracted from the PILS dataset convolved with a $24''$ beam.

Table 3. Upper limit column densities (N_{tot}) for the ^{13}C and deuterated isotopologues of CH_3CCH , as well as the H_2 abundance ratio, in IRAS 16293B and IRAS 16293A. The 3σ upper limits are determined using the excitation temperatures, FWHMs and H_2 column densities given in Table 2 for each source.

Molecule	N_{tot} (cm^{-2})	$\frac{N_{\text{tot}}}{N(\text{H}_2)}$
IRAS 16293 A		
$\text{CH}_3^{13}\text{CCH}$	$<2.44 \times 10^{14}$	$<3.87 \times 10^{-11}$
$^{13}\text{CH}_3\text{CCH}$	$<2.51 \times 10^{14}$	$<3.98 \times 10^{-11}$
$\text{CH}_3\text{C}^{13}\text{CH}$	$<2.51 \times 10^{14}$	$<3.98 \times 10^{-11}$
CH_3CCD	$<7.91 \times 10^{14}$	$<1.26 \times 10^{-10}$
CH_2DCCH	$<2.64 \times 10^{14}$	$<4.19 \times 10^{-11}$
IRAS 16293 B		
$\text{CH}_3^{13}\text{CCH}$	$<2.44 \times 10^{14}$	$<2.03 \times 10^{-11}$
$^{13}\text{CH}_3\text{CCH}$	$<2.51 \times 10^{14}$	$<2.09 \times 10^{-11}$
$\text{CH}_3\text{C}^{13}\text{CH}$	$<2.51 \times 10^{14}$	$<2.09 \times 10^{-11}$
CH_3CCD	$<7.91 \times 10^{14}$	$<6.59 \times 10^{-11}$
CH_2DCCH	$<2.64 \times 10^{14}$	$<2.20 \times 10^{-11}$

(CASA; McMullin et al. 2007) was used to convolve the PILS data with a $24''$ beam, to determine how much of the emission from the hot corino components could explain the emission detected in the IRAM 30m observations. Figure 3 shows a

Table 4. Spatial extent of different transitions of CH_3CCH towards each hot corino in the IRAS 16293 system.

Transition	E_{up}	Spatial extent [†]
IRAS 16293A		
$\text{CH}_3\text{CCH } 6\ 1 - 5\ 1$	24 K	$1.7''$ 233 au
$\text{CH}_3\text{CCH } 6\ 3 - 5\ 3$	82 K	$1.5''$ 214 au
$\text{CH}_3\text{CCH } 21\ 2 - 20\ 2$	218 K	$1.4''$ 200 au
$\text{CH}_3\text{CCH } 20\ 3 - 19\ 3$	237 K	$1.3''$ 185 au
IRAS 16293B		
$\text{CH}_3\text{CCH } 6\ 1 - 5\ 1$	24 K	$1.9''$ 259 au
$\text{CH}_3\text{CCH } 6\ 3 - 5\ 3$	82 K	$1.5''$ 203 au
$\text{CH}_3\text{CCH } 21\ 2 - 20\ 2$	218 K	$1.1''$ 148 au
$\text{CH}_3\text{CCH } 20\ 3 - 19\ 3$	237 K	$1.0''$ 145 au

Notes. [†]The spatial extent in au is calculated for a source distance of 141 pc as determined by Dzib et al. (2018).

Table 5. The initial fractional abundances with respect to the total hydrogen used in the three-phase chemical kinetics model *MAGICKAL*.

Species	Abundance
He	9.00×10^{-2}
N	7.50×10^{-5}
O	3.20×10^{-4}
H	2.00×10^{-3}
H_2	4.99×10^{-1}
C	1.40×10^{-4}
S^+	8.00×10^{-8}
Si^+	8.00×10^{-9}
Na^+	2.00×10^{-8}
Mg^+	7.00×10^{-9}
P^+	3.00×10^{-9}
Cl^+	4.00×10^{-9}

spectrum of CH_3CCH lines, extracted from the convolved PILS data. The lines are heavily contaminated with absorption effects, however, comparing these lines to the spectra in Figure 4 of Andron et al. (2018), the IRAM 30 m observations are $\sim 50\%$ brighter than the CH_3CCH emission found in the the PILS convolved observations. This suggests there is an additional cold component of CH_3CCH emission that is detected in the IRAM 30m observations, which is filtered out by the PILS dataset on scales larger than 2380 au.

4. Chemical modelling

To understand the results from this observational study in terms of the wider chemistry in IRAS 16293, chemical modelling of CH_3CCH was undertaken. The three-phase chemical kinetics model *MAGICKAL* (Garrod 2013; Willis & Garrod 2017) was used to model the formation and destruction pathways of CH_3CCH . It uses gas-phase, grain-surface and bulk ice reactions, using a chemical network based on that of Belloche et al. (2017). A two-stage physical model is used. Initially, the cold collapse stage has an isothermal gas temperature of 10 K, and the dust temperature cools from an initial value of 16 K to a final value of 8 K. This collapse takes 1.63×10^6 years. This is then followed by a static warm-up to 400 K. The chemical model is a single-point model, thus it has a uniform density. The initial abundances used in the code are given in Table 5. The cosmic-ray ionisation rate, ζ , is assumed to be $1.3 \times 10^{-17} \text{ s}^{-1}$, while the UV field has little effect during the hot-core stage due to high extinction. This model has been used previously to model CH_3CN and CH_3NC (Calcutt et al. 2018), and NH_2CN in IRAS 16293 (Coutens et al. 2018).

For this work, four models have been run to explore the solid-phase and gas-phase abundances of CH_3CCH at different final densities: $n_{\text{H}} = 1.6 \times 10^7, 6 \times 10^8, 6 \times 10^9$, and $6 \times 10^{10} \text{ cm}^{-3}$, shown in Figure 4. These correspond to the varying densities seen in the IRAS 16293 system, with the highest density corresponding to the continuum peak of IRAS 16293B, and the lowest density corresponding to the density of the filament between IRAS 16293A and IRAS 16293B (Jacobsen et al. 2018). The subsequent warm-up phase starts at a dust temperature of 8 K, and reaches a final temperature of 400 K at 2.8×10^5 years. This timescale is used to represent an intermediate-timescale warm-up, where 2×10^5 years is the time spent to reach a dust temperature of 200 K. This is taken from Garrod & Herbst (2006).

CH_3CCH has both grain-surface and gas-phase formation routes in the modelling. On the grains, it is formed first through

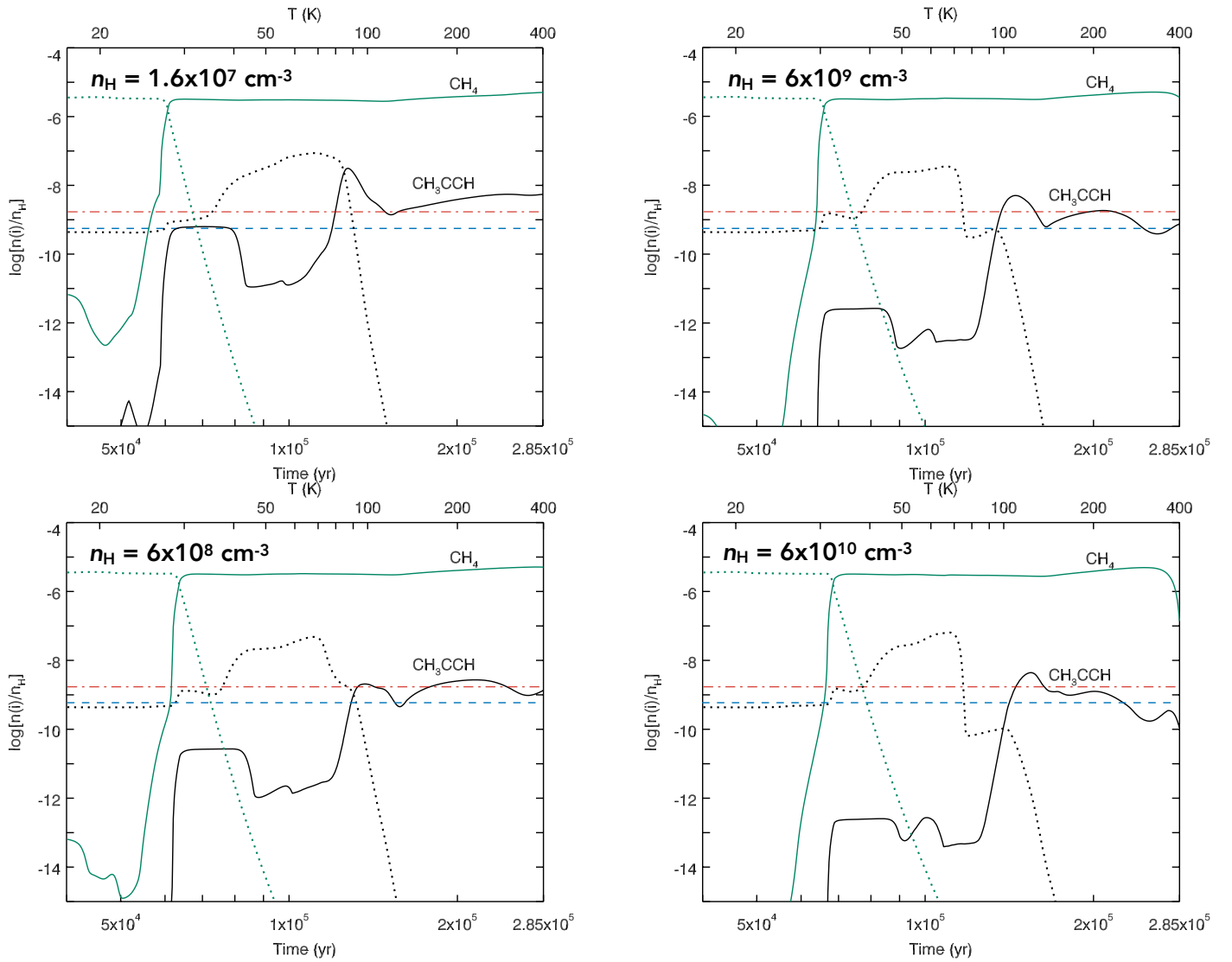


Fig. 4. Abundances of CH_3CCH derived from chemical modelling for the warm-up stage of a hot core type model. Each panel represents a model with a different final collapse density, ranging from $n_{\text{H}} = 1.6 \times 10^7 - 6 \times 10^{10} \text{ cm}^{-3}$. Solid lines denote gas-phase abundances, while dotted lines indicate grain-surface abundances. The red and blue dashed lines show the observational abundances in IRAS 16293A and B respectively.

successive hydrogenation of smaller hydrocarbons. This process begins with hydrogenation of C_3 . Hydrogenation of C_3 up to C_3H_2 proceeds without barrier, while hydrogenation of C_3H_2 has a small barrier of 250 K (Garrod 2013). Further hydrogenation to CH_3CCH proceeds without a barrier. Reaction of CH_3CCH with H on the grain-surfaces has a yet-higher barrier of 1510 K, so very little CH_3CCH is further hydrogenated at low temperatures (Tsang & Walker 1992). This is the primary destruction pathway for CH_3CCH on the grain-surface. At temperatures above 45 K hydrogen abstraction from abundant radicals such as OH, NH_2 , and CH_2OH also contributes to the destruction of CH_3CCH (Dean & Bozzelli 2000), leading to the formation of C_3H_3 and thus the formation of H_2O , NH_3 and CH_3OH .

In the gas-phase, the chemistry is more complex. CH_3CCH can form through neutral-neutral reactions, including $\text{C}_2\text{H}_4 + \text{CH} \rightarrow \text{H} + \text{CH}_3\text{CCH}$ (Loison et al. 2017). However, the primary gas-phase formation pathway used in the modelling is dissociative recombination of larger hydrocarbons (e.g. C_3H_5^+ , C_4H_5^+). Some of these larger hydrocarbons are formed in part from CH_3CCH , so for some larger hydrocarbons this pathway

becomes a feedback loop. However, for other larger hydrocarbons (as in the case of C_3H_5^+), they are formed almost exclusively from reactions of CH_4 with smaller hydrocarbons. The rates for these recombinations are taken from the OSU 2008 network (Garrod et al. 2008). Thus the increase in gas-phase abundance of CH_3CCH is directly tied to the desorption of CH_4 from the dust grains. CH_4 has a binding energy of 1300 K (Garrod & Herbst 2006).

CH_3CCH is destroyed in the gas-phase by abundant ions (e.g. H_3^+ , H^+ , HCO^+). The rates for these ion-molecule are calculated according to the method of Herbst & Leung (1986). An additional contribution to the destruction of CH_3CCH in the gas-phase comes from atomic C at $T > 40\text{K}$. The atomic C produces a carbon insertion reaction, lengthening the carbon backbone and ejecting H/ H_2 to form $\text{C}_4\text{H}_3/\text{C}_4\text{H}_2$, respectively. The rates for these reactions are taken from Harada et al. (2010).

The abundance of methane compared to the abundance of propyne in the different density models is shown in Figure 4. CH_4 desorbs from the grains at slightly higher temperatures in the high density models. In the lowest density model, it desorbs

at about 26–27 K, while in the highest density model, it desorbs at about 32 K. This means that the low-temperature abundance peak is higher for CH₃CCH in the lower density models, as there is more CH₄ at earlier times in the gas-phase.

In general, the grain-surface chemistry is what controls the final abundance of propyne. However, there are some key differences between the models. In the higher-density models, the grain-surface abundance of CH₃CCH decreases sharply before it desorbs from the grains. This is due to the larger abundance of atomic H on the grains at higher densities, which leads to more efficient hydrogenation of propyne to C₃H₅. After this point, propyne desorbs from the grains, and the change in gas-phase abundance of CH₃CCH is similar between the different models, all showing a slight dip in abundance at higher temperatures, which is more pronounced in the higher density model. This is due to propanal (C₂H₅CHO), which is slightly more abundant in the gas-phase in the lower-density models. Protonated propanal can recombine to form CH₃CCH.

In the lower-density models, there is a larger amount of methane (CH₄), which is converted into larger hydrocarbons that then recombine and feed into the abundance of propyne. This is responsible for the difference in the level of abundance at ~30 K in the models, and that heavily influences the later behaviour as well. This primarily has an impact on the gas-phase abundances in the models, whereas the peak grain-surface abundances do not vary significantly between the different models. Methane is predominantly formed on grains, through the hydrogenation of C. At higher temperatures, methane is also produced as a product of the CH₃ radical abstracting H atoms from species such as H₂ and H₂CO (Baulch et al. 1992). The CH₃ radical is formed primarily from dissociation of CH₃OH by cosmic-rays. The rate of dissociation is computed in the model to be $4.6 \times 10^{-15} \text{ s}^{-1}$, assuming a canonical cosmic-ray ionisation rate of $1.3 \times 10^{-17} \text{ s}^{-1}$ in our network.

5. Discussion

The results from this study highlight how CH₃CCH emission in IRAS 16293A and IRAS 16293B is similar, both in spatial extent and abundance. To put this result in the wider context of chemistry in hot corinos/hot cores, it is important to compare it to similar studies in other sources. Whilst CH₃CCH has been detected in a variety of objects throughout the Galaxy, there are not many sources where the abundances have been determined with a high enough angular resolution, to ensure abundances are not heavily affected by beam dilution issues. One such high angular resolution study was performed recently of the high-mass hot core in the source AFGL 4176 by Bøgelund et al. (2019). Their study used ALMA observations to explore the continuum emission and the molecular content of AFGL 4176. The observed excitation temperatures and abundances of different molecules were then compared with a variety of sources, including IRAS 16293. In some cases, such as for CH₃CN, NH₂CHO, C₂H₅OH, CH₃OCH₃, CH₃OCHO and (CH₂OH)₂, abundances were found to be very similar between AFGL 4176 and IRAS 16293B. However, for CH₃CHO, CH₃COCH₃, C₂H₃CN, C₂H₅CN, H₂CS, and SO₂ the abundances were notably different. The excitation temperatures found for these molecules in AFGL 4176 and IRAS 16293B also varied greatly, showing no correlation with the abundance similarities seen for some molecules. CH₃CCH was detected in the AFGL 4176 study but is 6 times more abundant relative to CH₃OH than in IRAS 16293B and 12 times more abundant relative to CH₃OH than in IRAS 16293A. It also has a higher excitation temperature of 320 K in AFGL 4176.

Most notable, however, is the difference in spatial scale traced by CH₃CCH in AFGL 4176. The brightest continuum peak in the source, mm1, is coincident with the bulk of the complex organic molecule emission, with the exception of CH₃CCH. CH₃CCH has a double peaked morphology in the source, peaking both near the mm1 continuum peak position and at a second continuum peak, mm2, which is located north-west of mm1. A third continuum peak, mm3, is also seen in this source, located south-east of mm1. AFGL 4176-mm2 and -mm3 are located perpendicular to the major axis of mm1 and may be indicative of a large-scale outflow, which is consistent with the CO observations presented by Johnston et al. (2015). This outflow could be responsible for the double-peaked morphology of CH₃CCH. Its emission, however, was not analysed towards mm3 to verify this possibility (Bøgelund, private communication).

Fayolle et al. (2015) performed an observational study of massive young stellar objects (MYSOs) with weak hot organic emission lines. Data from the IRAM 30 m and the Submillimeter Array (SMA), were used to determine molecular abundances towards three MYSOs, NGC 7538 IRS9, W3 IRS5, AFGL490, with known ice abundances, but without luminous molecular hot cores. They found that in contrast to other complex molecules, little or no CH₃CCH flux from the IRAM observations was recovered by the SMA observations, indicating an extended emission, which was spatially filtered by the SMA observations. This emission could have been large-scale emission and/or off-centred emission.

The differences observed in the spatial emission of CH₃CCH compared to other molecules observed by both Fayolle et al. (2015) and Bøgelund et al. (2019) suggest that CH₃CCH has a more complicated story than many other complex molecules. In contrast, its emission in IRAS 16293 does trace compact scales, tracing the hot corino components in both IRAS 16293A and IRAS 16293B up to scales of ~2000 au, in addition to larger scale emission indicated by the IRAM 30 m observations discussed in Section 3.2. It is likely that the combination of both gas-phase and grain-surface pathways to the formation of CH₃CCH means that it is a ‘gateway’ molecule tracing the interface between the hot corino region and the colder lower envelope, as well as tracing the larger colder envelope as is seen in the IRAM 30 m observations.

6. Summary and conclusions

In this study, an analysis of CH₃CCH chemistry was undertaken, using high angular resolution ALMA observations towards the two forming protostars in the IRAS 16293 system. Bright lines of CH₃CCH are detected towards both IRAS 16293A and IRAS 16293B, with upper energy levels ranging from 17 to 449 K. The excitation temperatures and abundances derived through LTE modelling, are similar in both sources. The 90–100 K excitation temperatures are comparable to the excitation temperatures of several other molecules detected in these sources.

These data show that CH₃CCH emission has a FWHM of ~1–2'' (~145–260 au) around each source, indicating that this molecule is tracing the hot corino component in this dataset. This is similar to the spatial scale traced by other complex organic molecules, such as methyl cyanide and methyl formate in both sources. Lines with a lower upper energy level trace a slightly larger spatial scale.

The CH₃CCH emission found in this work was convolved with a 24'' beam, to determine whether the emission found in previous single dish studies in IRAS 16293, could be due solely

to the two hot corino components. Spectra extracted from the convolved PILS dataset was 50% weaker than previous IRAM 30 m observations, indicating an additional cold component of propyne emission is present in the single-dish data. This cold component is not detected in the PILS dataset, which is likely due to it tracing larger scales (>2380 au) than the largest angular scale of the observations, and hence being filtered out.

In addition to our observations, chemical modelling of CH₃CCH in IRAS 16293 was performed using the three-phase chemical kinetics model *MAGICKAL*. The modelling has found that to form enough CH₃CCH to match the observational abundances, a complex chemistry of both gas-phase and grain-surface reactions is required. On the grains, it is formed first through successive hydrogenation of smaller hydrocarbons. In the gas-phase, its primary formation pathway is dissociative recombination of larger hydrocarbons (e.g. C₃H₅⁺, C₄H₅⁺; Garrod 2013). These larger hydrocarbons are formed through reactions of CH₄ with smaller hydrocarbons. Thus, the increase in gas-phase abundance of CH₃CCH is directly tied to the abundance of CH₄, which correlates strongly with the final collapse density of the model.

The emission of CH₃CCH in IRAS 16293 was also compared to its emission in several high-mass star-forming regions. In the hot core AFGL 4176, the emission traces multiple continuum peaks in the data, which contrasts with the scale traced by other complex organic molecules detected towards the source. In several other massive young stellar objects (MYSOs), with weak hot organic emission lines, CH₃CCH emission is found only on larger scales. The multiple scales traced by CH₃CCH are also seen in IRAS 16293, highlighting the complicated physical structures traced by this molecule. These differences are likely driven by a strong gas-phase and grain-surface chemistry leading to abundant CH₃CCH formation in different environments.

CH₃CCH is an important complex organic molecule, whose presence in star-forming regions can be used to understand the temperature conditions around forming stars. This, combined with the large number of regions in both the Galaxy and beyond where it has been detected, offers an opportunity to compare how the chemistry varies across different objects, and explore the reasons for this variability. However, it is clear that the complicated chemistry that forms CH₃CCH allows it to be present on multiple scales. It is crucial that its physical structure is taken into account when determining its abundances and excitation temperatures, if it is to function as a benchmark molecule for different star-forming regions.

Acknowledgements. The authors would like to thank the referee for their helpful comments on the manuscript. The authors would like to acknowledge the European Union whose support has been essential to this research. In particular a European Research Council (ERC) grant, under the Horizon 2020 research and innovation programme (grant agreement No. 646908) through ERC Consolidator Grant “S4F” to J.K.J. AC postdoctoral grant is funded by the ERC Starting Grant 3DICE (grant agreement 336474). S.F.W. acknowledges financial support from the Swiss National Science Foundation (SNSF) Eccellenza Professorial Fellowship PCEFP2_181150. MND is supported by the Swiss National Science Foundation (SNSF) Ambizione grant 180079, the Center for Space and Habitability (CSH) Fellowship and the IAU Gruber Foundation Fellowship. This paper makes use of the following ALMA data: ADS/JAO.ALMA#2013.1.00278.S and ADS/JAO.ALMA#2012.1.00712.S. ALMA is a partnership of ESO (representing its member states), NSF (USA) and NINS (Japan), together with NRC (Canada) and NSC and ASIAA (Taiwan), in cooperation with the Republic of Chile. The Joint ALMA Observatory is operated by ESO, AUI/NRAO and NAOJ. This research has made use of NASA’s Astrophysics Data System. This research has also made use of Astropy,² a community-developed core Python package for Astronomy (Astropy Collaboration et al. 2013, 2018).

References

- Andron, I., Gratier, P., Majumdar, L., et al. 2018, *MNRAS*, 481, 5651
- Astropy Collaboration, Price-Whelan, A. M., Sipőcz, B. M., et al. 2018, *AJ*, 156, 123
- Astropy Collaboration, Robitaille, T. P., Tollerud, E. J., et al. 2013, *A&A*, 558, A33
- Baulch, D. L., Cobos, C. J., Cox, R. A., et al. 1992, *Journal of Physical and Chemical Reference Data*, 21, 411
- Behrard, A., Fayolle, E. C., Graninger, D. M., et al. 2019, *ApJ*, 875, 73
- Belloche, A., Meshcheryakov, A. A., Garrod, R. T., et al. 2017, *A&A*, 601, A49
- Bögelund, E. G., Barr, A. G., Taquet, V., et al. 2019, *A&A*, 628, A2
- Calcutt, H., Fiechter, M. R., Willis, E. R., et al. 2018, *A&A*, 617, A95
- Calcutt, H., Jørgensen, J. K., Müller, H. S. P., et al. 2018, *A&A*, 616, A90
- Cazaux, S., Tielens, A. G. G. M., Ceccarelli, C., et al. 2003, *ApJ*, 593, L51
- Cazzoli, G. & Pazzarini, C. 2008, *A&A*, 487, 1197
- Chandler, C. J., Brogan, C. L., Shirley, Y. L., & Loinard, L. 2005, *ApJ*, 632, 371
- Collings, M. P., Anderson, M. A., Chen, R., et al. 2004, *MNRAS*, 354, 1133
- Cordiner, M. A., Palmer, M. Y., Nixon, C. A., et al. 2015, *ApJ*, 800, L14
- Coutens, A., Jørgensen, J. K., van der Wiel, M. H. D., et al. 2016, *A&A*, 590, L6
- Coutens, A., Willis, E. R., Garrod, R. T., et al. 2018, *A&A*, 612, A107
- Dean, A. M. & Bozzelli, J. W. 2000, Springer, 125
- Dzib, S. A., Ortiz-León, G. N., Hernández-Gómez, A., et al. 2018, *A&A*, 614, A20
- Endres, C. P., Schlemmer, S., Schilke, P., Stutzki, J., & Müller, H. S. 2016, *Journal of Molecular Spectroscopy*, 327, 95, new Visions of Spectroscopic Databases, Volume II
- Fayolle, E. C., Öberg, K. I., Garrod, R. T., van Dishoeck, E. F., & Bisschop, S. E. 2015, *A&A*, 576, A45
- Garrod, R. T. 2013, *ApJ*, 765, 60
- Garrod, R. T. & Herbst, E. 2006, *A&A*, 457, 927
- Garrod, R. T., Widicus Weaver, S. L., & Herbst, E. 2008, *ApJ*, 682, 283
- Harada, N., Herbst, E., & Wakelam, V. 2010, *ApJ*, 721, 1570
- Harada, N., Sakamoto, K., Martín, S., et al. 2018, *ApJ*, 855, 49
- Herbst, E. & Leung, C. M. 1986, *ApJ*, 310, 378
- Hernández-Gómez, A., Loinard, L., Chandler, C. J., et al. 2019, *ApJ*, 875, 94
- Jacobsen, S. K., Jørgensen, J. K., van der Wiel, M. H. D., et al. 2018, *A&A*, 612, A72
- Johnston, K. G., Robitaille, T. P., Beuther, H., et al. 2015, *ApJ*, 813, L19
- Jørgensen, J. K., Müller, H. S. P., Calcutt, H., et al. 2018, *A&A*, 620, A170
- Jørgensen, J. K., van der Wiel, M. H. D., Coutens, A., et al. 2016, *A&A*, 595, A117
- Le Guennec, M., Demaison, J., Włodarczyk, G., & Marsden, C. J. 1993, *Journal of Molecular Spectroscopy*, 160, 471
- Ligterink, N. F. W., Coutens, A., Kofman, V., et al. 2017, *MNRAS*, 469, 2219
- Loison, J.-C., Agúndez, M., Wakelam, V., et al. 2017, *MNRAS*, 470, 4075
- Lykke, J. M., Coutens, A., Jørgensen, J. K., et al. 2017, *A&A*, 597, A53
- Manigand, S., Calcutt, H., Jørgensen, J. K., et al. 2019, *A&A*, 623, A69
- Martín, S., Mauersberger, R., Martín-Pintado, J., Henkel, C., & García-Burillo, S. 2006, *ApJS*, 164, 450
- McMullin, J. P., Waters, B., Schiebel, D., Young, W., & Golap, K. 2007, in *Astronomical Society of the Pacific Conference Series*, Vol. 376, *Astronomical Data Analysis Software and Systems XVI*, ed. R. A. Shaw, F. Hill, & D. J. Bell, 127
- Müller, H. S. P., Pracna, P., & Horneman, V. M. 2002, *Journal of Molecular Spectroscopy*, 216, 397
- Müller, H. S. P., Thorwirth, S., Bizzocchi, L., & Winnewisser, G. 2000, *Zeitschrift Naturforschung Teil A*, 55, 491
- Pech, G., Loinard, L., Chandler, C. J., et al. 2010, *ApJ*, 712, 1403
- Pineda, J. E., Maury, A. J., Fuller, G. A., et al. 2012, *A&A*, 7, 3
- Snyder, L. E. & Buhl, D. 1973, *Nature Physical Science*, 243, 45
- Snyder, L. E., Lovas, F. J., Hollis, J. M., et al. 2005, *ApJ*, 619, 914
- Taniguchi, K., Saito, M., Majumdar, L., et al. 2018, *ApJ*, 866, 150
- Tsang, W. & Walker, J. A. 1992, *J. Chem. Phys.*, 96, 8378
- Willis, E. R. & Garrod, R. T. 2017, *ApJ*, 840, 61

² <http://www.astropy.org>